nature chemistry

Article

https://doi.org/10.1038/s41557-025-01810-2

Synthesis of zwitterionic open-shell bilayer spironanographenes

Received: 23 April 2024

Accepted: 24 March 2025

Published online: 30 April 2025

Check for updates

Juan Lión-Villar[1], Jesús M. Fernández-García[1], Samara Medina Rivero[2], Josefina Perles[3], Shaofei Wu[4], Daniel Aranda[2], Jishan Wu[4], Shu Seki[5], Juan Casado[2] ✉ & Nazario Martín[1,6] ✉

Molecular nanographenes (NGs) are nanoscale graphene fragments obtained by organic synthetic protocols. Here we report the bottom-up synthesis of two spiro-NGs formed by two substituted hexa-*peri*-hexabenzocoronenes (HBCs), spiro-NG and F-spiro-NG. The X-ray crystal structure of the deca-*tert*-butyl-functionalized spiro-NG shows a bilayer disposition of the HBCs in face-to-face contact. By contrast, F-spiro-NG, which features *tert*-butyl substituents on one HBC unit, and fluorine on the other HBC unit, is an electron donor–acceptor bilayer NG. The structural assembly of the donor and acceptor graphenic layers enables an electron-transfer process that leads to the formation of a zwitterionic open shell, paramagnetic species constituted by a radical cation and a radical anion located in the donor and the acceptor HBCs, respectively. Magnetic and spectroelectrochemical experiments, together with theoretical calculations, support the persistent/dominant charge-separated nature of F-spiro-NG. Furthermore, photoconductivity measurements show a significant increase of the charge carrier mobility in the case of F-spiro-NG ($\Sigma\mu = 6\ cm^2\ V^{-1}\ s^{-1}$) compared with spiro-NG.

Aviram and Ratner laid the foundations of molecular electronics in 1974, when they theorized a molecular rectifying diode as a p–n junction semiconductor based on donor–spacer–acceptor molecules[1]. Since then, σ- or π-bridged molecular donor–acceptor systems became essential for the development of optoelectronic applications involving artificial photosynthesis[2,3], photovoltaic devices[4,5] and semiconducting and conducting materials[6–9], among others.

Simultaneously, in the seventies, the field of organic charge-transfer complexes emerged with the preparation of the key tetrathiafulvalene–7,7,8,8-tetracyano-*p*-quinodimethane organic conductor under the name of synthetic metals[10,11], nowadays referred to as organic electronics[12–14]. The extension of the electron transfer in charge-transfer organic salts depends on the ionization potential of the donor and on the electron affinity of the acceptor[15]. However, other factors such as the separation and nature of the intermolecular overlap of the two moieties also play a decisive role[16,17]. More recently, the discovery of the so-called frustrated radical pairs has enabled the development of new synthetic strategies taking profit from transient-to-persistent charge-separated (radical-ion) states in sterically hindered complexes[18,19]. Organic synthesis has enabled precise tuning of the donor–acceptor character by combining electron-rich and electron-deficient units and modulating the steric effects involved. However, in these supramolecular structures, control over the structural orientation of the components is limited.

As an alternative to supramolecular engineering of interchromophore ordering, covalent strategies have been developed[20–22]. In this way, taking advantage of the synthetic control delivered by the bench-top bottom-up synthesis of molecular nanographenes (NGs)[23–30], we

[1]Departamento de Química Orgánica I, Facultad de Ciencias Químicas, Universidad Complutense de Madrid, Madrid, Spain. [2]Departamento de Química-Física, Facultad de Ciencias, Universidad de Málaga, Málaga, Spain. [3]Laboratorio DRX Monocristal, SIdI, Universidad Autónoma de Madrid, Madrid, Spain. [4]Department of Chemistry, National University of Singapore, Singapore, Singapore. [5]Department of Molecular Engineering, Kyoto University, Kyoto, Japan. [6]IMDEA-Nanociencia, Madrid, Spain. ✉e-mail: casado@uma.es; nazmar@ucm.es

https://doi.org/10.1038/s41557-025-01810-2

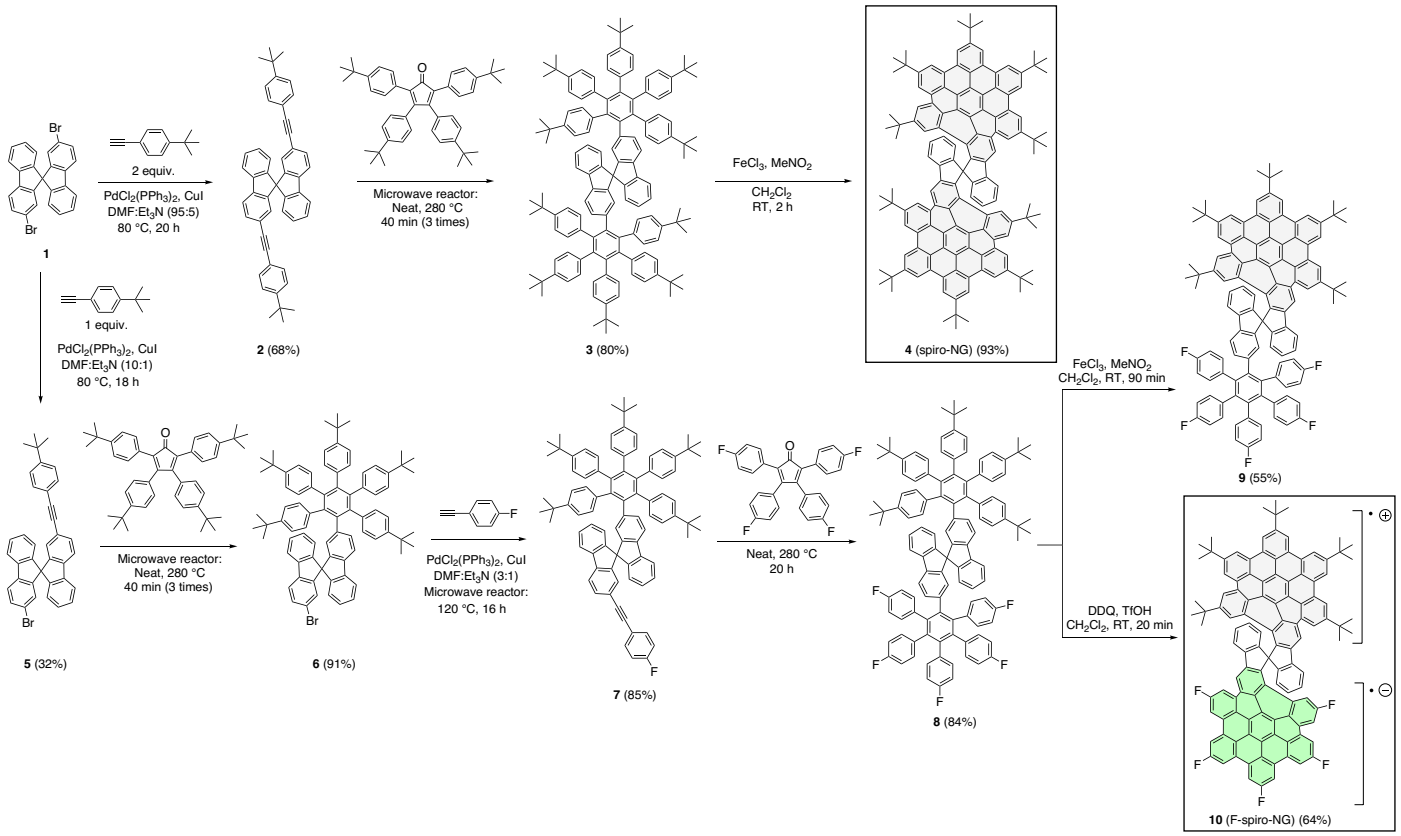

Fig. 1 | Synthetic route towards spiro-NGs. Synthetic pathway of ᵗBu-substituted spiro-NG (**4**), partially graphitized intermediate **9** and fully graphitized donor–acceptor fluorine-substituted F-spiro-NG (**10**). Molecules are depicted in their planar configuration for clarity, but the structural aspects are discussed in detail in the main text. RT, room temperature; DMF, dimethylformamide.

have developed NG stacked bilayers controlling the relative orientation of two hexa-*peri*-hexabenzocoronenes (HBCs) by the presence of [*n*] helicene connectors[31]. In these examples, helicenes of different lengths have been utilized to fix the structure, separation and orientation of the bilayer NGs, resulting in constructs that evolve from negligible interlayer coupling to face-to-face coupling with strong through-space intramolecular exciton and charge delocalization.

Here we report a NG structure constructed by the π-extension of a spirobifluorene core, leading to two HBCs linked by a spirocycle. In contrast to the orthogonal geometry previously reported for HBCs[32], spiro-NG consists of a distorted bilayer with close face-to-face orientation of the HBC layers. Inspired by this geometry, we synthesized another bilayer NG, F-spiro-NG, which features five *tert*-butyl groups in one HBC layer and five fluorine atoms in the other. This led to the formation of a donor–acceptor bilayer NG (F-spiro-NG). Interestingly, the structural distortion undergone by the spirobifluorene core leads to an efficient intramolecular single electron transfer between the donor and the acceptor HBCs with the formation of a stable zwitterionic open-shell radical-ion species. Theoretical calculations, electron paramagnetic resonance (EPR) and spectroelectrochemical studies underpin the existence of the charge-separated state. Furthermore, a remarkable charge carrier mobility ($\Sigma\mu = 6\ cm^2\ V^{-1}\ s^{-1}$) is shown by this donor–acceptor bilayer NG.

Synthetic procedure

Spiro-NG (**4**) was prepared following a multistep synthetic protocol for the π-extension of aromatic scaffolds commonly used in the preparation of molecular NGs[33–40], followed by a final graphitization step (Fig. 1)[41–43]. The first reaction consisted of a double Pd-catalysed Sonogashira cross-coupling between commercially available 2,2′-dibromo-9,9′-spirobi[9*H*-fluorene] (**1**) and 4-*tert*-butylphenylacetylene, affording the dialkynylated spirobifluorene **2** in 68% yield. Thereafter, a double [4 + 2] Diels–Alder cycloaddition, followed by a CO cheletropic extrusion, using tetrakis-(4-*tert*-butylphenyl)cyclopentadienone as diene, led to oligoarene **3**. Finally, a Scholl dehydrogenative reaction with $FeCl_3$ as oxidant, in which the graphitization of **3** occurred, afforded the final spiro-NG **4** in 93% yield. It is worth mentioning that the readily synthetic pathway, consisting of three steps with an overall 51% yield, makes this process easily scalable.

For the synthesis of the donor–acceptor F-spiro-NG (**10**), only one equivalent of 4-*tert*-butylphenylacetylene was added in the first step. The resulting monoalkynylated spiro compound **5** was π-extended to oligoarene **6**, which contained five *tert*-butyl groups. Thus, a second Sonogashira cross-coupling with 4-fluorophenylacetylene gave the fluorinated alkyne **7**, which was π-extended again to the pentafluorinated oligoarene **8** by following the standard protocol (Fig. 1). Two different products were obtained depending on the Scholl reaction conditions used. Using $FeCl_3$ as Lewis acid, compound **9**, in which the *tert*-butyl-substituted HBC was graphitized, could be isolated in 55% yield, together with minor amount of totally graphitized **10**. By contrast, by using 2,3-dichloro-5,6-dicyano-1,4-benzoquinone (DDQ) as oxidant, a further extension of the Scholl reaction gave rise solely to F-spiro-NG (**10**). This NG was obtained as a deep-green solid in a 64% yield. High-resolution mass spectrometry by atmospheric pressure chemical ionization (APCI) of F-spiro-NG showed the expected exact mass (calculated for $C_{117}H_{75}F_5$(-H): 1,573.5710, found: 1,573.5701). Raman spectroscopy revealed the graphene-like nature of F-spiro-NG, showcasing the presence of D and G bands at wave numbers that closely align with those of spiro-NG (Supplementary Fig. 75). Notably, F-spiro-NG was

https://doi.org/10.1038/s41557-025-01810-2

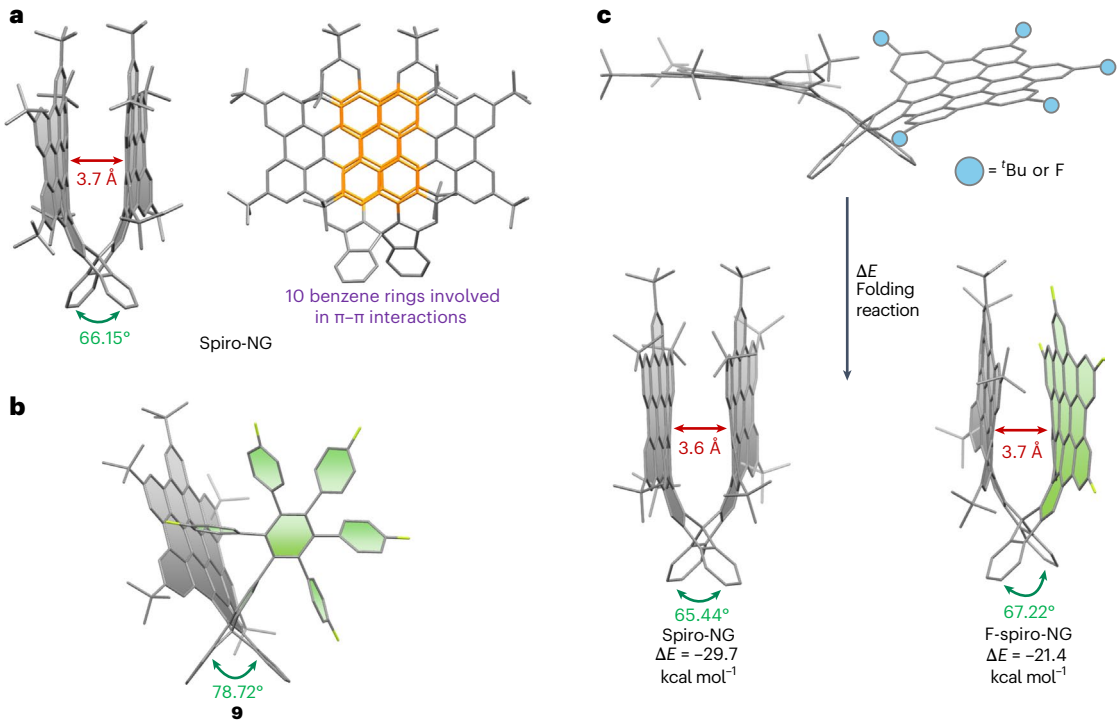

Fig. 2 | Structural analysis. a, The molecular structure of compound spiro-NG (**4**) obtained by SCXRD (hydrogen atoms have been omitted for clarity) (lateral view, top left; zenithal view, top right). **b**, The molecular structure of compound **9** obtained by SCXRD (hydrogen atoms have been omitted for clarity). **c**, Optimized structures and folding reactions for spiro-NG and F-spiro-NG (DFT/CAM-B3LYP-D3/6-31G** level). Interlayer distances are given in ångströms (red arrows), and twisting angles of the spirobifluorene moiety are given in degrees (green arrows).

Table 1 | Optical properties measured in dichloromethane at room temperature and redox potential values obtained from square-wave voltammetry versus Fc/Fc^+, measured in toluene–acetonitrile at room temperature

	λ_{abs}, nm (ε, $M^{-1}cm^{-1}$)	λ_{em}, nm (shoulder)	E_{ox}, V	E_{red}, V
4 (spiro-NG)	368 (287,800), 408 (93,400), 452 (6,100), 480 (2,600)	482, 503, 514, (540), (550)	0.57, 0.78	−2.37
10 (F-spiro-NG)	368 (94,300), 452 (24,400), 480 (13,100), 490 (11,300), 624 (5,900), 939 (4,500)	478, (490), 507, (513), (540)	0.42, 0.87	−0.42, −1.53, −2.42

NMR silent, suggesting a paramagnetic character that was subsequently confirmed by EPR studies.

Single-crystal X-ray diffraction and structural modelling

Centrosymmetric racemic crystals of spiro-NG (**4**), containing both *M* and *P* isomers, were obtained through vapour diffusion of methanol into a spiro-NG solution in dichloromethane, allowing its structure to be solved by single-crystal X-ray diffraction (SCXRD) (Fig. 2a). The molecule of spiro-NG shows an unexpected U shape where the two HBCs are parallel to each other and placed as close as possible to maximize their overlap, while the benzene rings of the spirobifluorene embedded in the HBC units are bent to allow the maximal interlayer contacts. Indeed, five benzenoid rings—a perylene subunit—in each layer are intensively involved in π–π interactions in an overlapped AA-stacking mode with an average distance of 3.70 Å between the centroids of a layer and the ones in the opposite plane (Supplementary Fig. 2). Another notable feature is the dihedral angle of 66.15°—the lowest one reported among spirobifluorene systems[44]—between the mean planes calculated for the atoms in the two bridging fluorenes (Supplementary Fig. 4), that further adopt a slightly twisted disposition. This energy-consuming deviation from the commonly found spirobifluorene perpendicular disposition is compensated by the large number of intramolecular (π–π and C–H···π) interactions formed in the overlap disposition between the HBC layers.

Quantum chemical calculations have been performed at the density functional theory (DFT)/CAM-B3LYP-D3/6-31G** level of theory for spiro-NG (Fig. 2c). Theory accurately predicts its experimental molecular structure by capturing the formation of close π–π contacts at distances of 3.6 Å as well as the 65.44° spirobifluorene twisting (that is, 3.7 Å and 66.15°, respectively, in the SCXRD analysis). The strength of these interactions, which acts as the driving force to reduce the spirobifluorene angle from 90° to 66.15°, has been theoretically evaluated by calculating the energy difference (ΔE) between the unfolded and the folded forms of spiro-NG. This energy difference is −29.7 kcal mol^{-1}, while the energy consumption for the twisting of the spirobifluorene unit is +20.1 kcal mol^{-1} (Supplementary Fig. 10).

The crystal structure for F-spiro-NG could not be obtained. Fortunately, the molecular structure of its precursor, compound **9**, which presents the ^{t}Bu-substituted HBC layer graphitized, has been solved by SCXRD (Fig. 2b). We clearly observe the twisting of the spiro-moiety, which amounts to 78.72°, an intermediate value between the 90° of spirobifluorene and the 67.22° in the CAM-B3LYP-D3/6-31G** optimized structure of F-spiro-NG (Fig. 2c).

Calculations carried out in vacuum at our level of theory reveal a stabilization energy (ΔE = −21.4 kcal mol^{-1}) of the folded form of F-spiro-NG compared with the open form, considering both structures as closed-shell configurations to be comparable. Furthermore, the singlet closed-shell form of F-spiro-NG is predicted to be more stable

https://doi.org/10.1038/s41557-025-01810-2

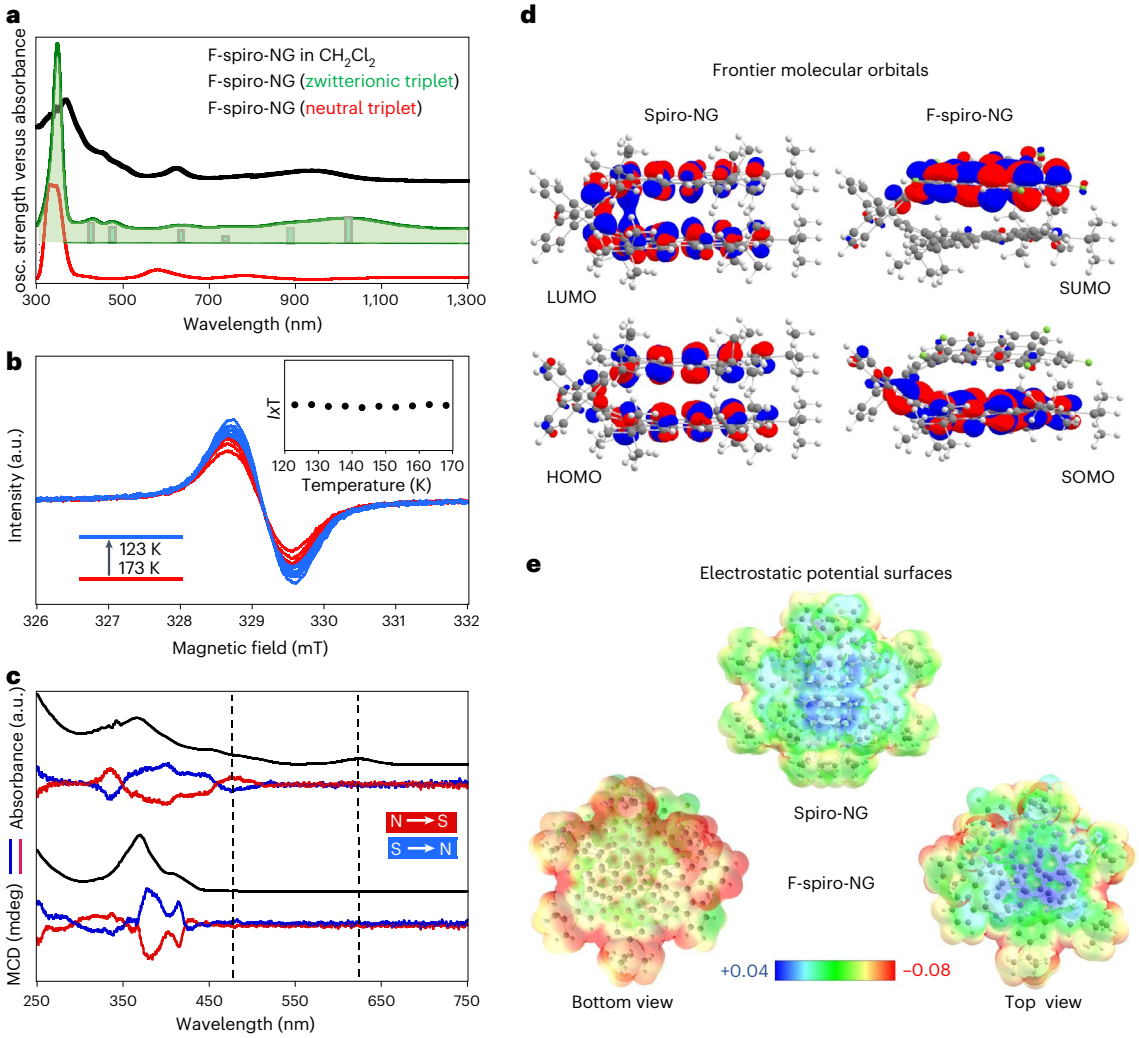

Fig. 3 | Spectroscopic properties and calculations. a, UV–vis–NIR electronic absorption spectrum of F-spiro-NG dissolved in CH_2Cl_2 at 298 K (black line) together with the TD-DFT/CAM-B3LYP-D3/6-31G** theoretical spectra simulated as a neutral triplet (red line) and as a charge-separated triplet (green line). osc. strength, oscillator strength. **b**, EPR spectra of F-spiro-NG in toluene. The inset represents the integrated intensity of the EPR signal of F-spiro-NG in toluene as a function of the temperature. **c**, MCD spectra of F-spiro-NG (top) and spiro-NG (bottom) in CH_2Cl_2 at 298 K, together with the corresponding UV–visible electronic absorption spectra (black lines). The blue and red lines correspond to the MCD spectra recorded with opposite orientations of the external magnetic field of 1 T. **d**, Orbital topologies of spiro-NG and F-spiro-NG. **e**, Electrostatic potential surfaces calculated at the DFT/CAM-B3LYP-D3/6-31G** level of theory for spiro-NG and F-spiro-NG.

than its open-shell triplet structure. However, this state is not able to satisfactorily account for the experimental evidence (NMR silent, EPR active). Alternatively, the simulation of the triplet state with neat charge separation within the donor–acceptor bilayer accurately reproduces all the experimental data, thus becoming the pivotal state in our research. To simulate such charge-separated state as the ground state, we resort to include an external electric field able to dissociate the charge given the challenging nature of open-shell zwitterionic states for DFT methods. In addition, by conducting calculations including solvent effects, a reduction of the closed shell/open shell energy difference is found, a situation that is more accentuated when the polarity of the solvent is increased. These findings reveal that π–π interactions are mostly kept in the triplet state whereas the energy consumption to form the open-shell zwitterionic state is compensated by the electrostatic stabilization in the charged radical pair. A similar charge separation reaction has been documented in supramolecular perylene dimers that are stabilized in the eclipsed AA face-to-face coupling by 5–9 kcal mol^{-1} at intermolecular distances of 3.5 Å. These supramolecular perylene assemblies can undergo photo-induced symmetry breaking charge-transfer reactions forming transient radical anions and cations[45–51] In this context, the predesigned symmetry breaking by the donor–acceptor structure of F-spiro-NG is the seed to promote the stabilization of the zwitterionic radical pair triplet state.

Optical and magnetic properties and electronic structure

The ultraviolet (UV)–visible absorption spectra of both NGs were measured in dichloromethane (Table 1 and Supplementary Figs. 11 and 12). Both molecules show a similar main electronic transition band in the UV region at 368 nm. In the visible region, spiro-NG shows a shoulder at 408 nm and two weak bands due to forbidden transitions at 452 and 480 nm. Conversely, F-spiro-NG presents these bands at 452 and 480 nm with medium intensity, therefore belonging to allowed electronic transitions with molar extinction coefficient values of 24,400 and 13,100 M^{-1} cm^{-1}, respectively. In contrast to spiro-NG, the spectrum of F-spiro-NG shows two bands in the visible–near-infrared (NIR) region, one at 624 nm together with a broader band centred at 939 nm.

The absorption spectra of spiro-NG (closed-shell configuration) and F-spiro-NG (zwitterionic triplet configuration) have been theoretically evaluated by time-dependent density functional theory (TD-DFT)

https://doi.org/10.1038/s41557-025-01810-2

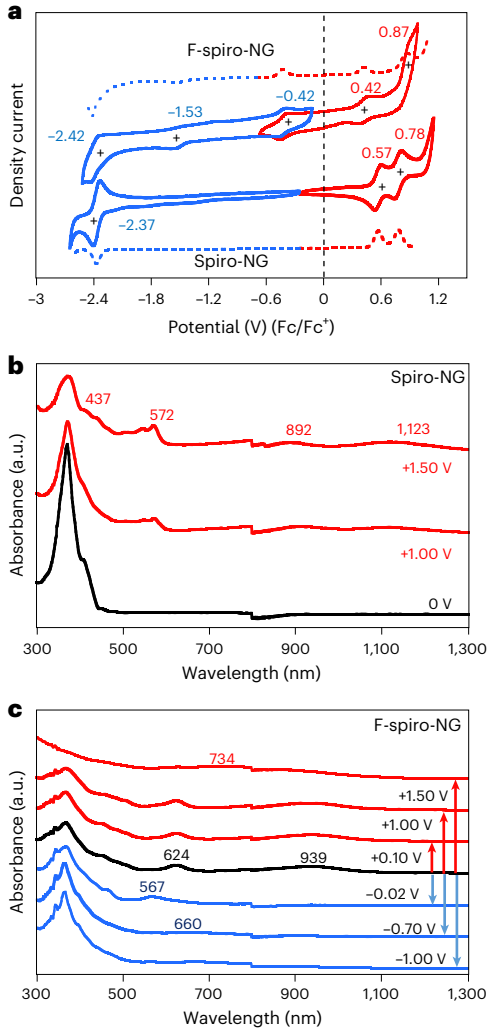

Fig. 4 | Electrochemistry and spectroelectrochemistry. a, Cyclic (solid lines) and square-wave (dashed lines) voltammograms of spiro-NG (bottom) and F-spiro-NG (top) versus Fc/Fc^+ measured in toluene–acetonitrile at 298 K. **b**, UV–visible–NIR electronic absorption spectra of spiro-NG obtained after oxidation (red) in Bu_4NPF_6 0.1 M in CH_2Cl_2 at 298 K. **c**, UV–visible–NIR electronic absorption spectra of F-spiro-NG obtained after oxidation (red) and reduction (blue) in Bu_4NPF_6 0.1 M in CH_2Cl_2 at 298 K. See potentials and characteristic bands as inserted values. The arrows indicate the step of the redox process.

calculations. For spiro-NG, the strong band experimentally found at 368 nm is very well simulated by the presence of several theoretical excitations (Supplementary Fig. 18a). Meanwhile, the theoretical UV–visible–NIR spectrum of the charge-separated (zwitterionic) triplet state of F-spiro-NG gives very good account of the whole experimental absorption (Fig. 3a). Indeed, the 624-nm band of F-spiro-NG discloses clear charge-transfer character associated with partial excitations between the singly occupied molecular orbital (SOMO) and singly unoccupied molecular orbital (SUMO) orbitals. Furthermore, the EPR spectrum of F-spiro-NG (Fig. 3b) shows a single-line signal ($g = 2.0027$) associated to a paramagnetic species (that is, the triplet excited state), accounting for two non-interacting—or weakly coupled—monoradicals. The product of the EPR intensity by the temperature (IT) as a function of the temperature (T) exhibits a constant behaviour that further indicates that the paramagnetic state is not in thermal equilibrium with any other non-paramagnetic or diamagnetic state in that temperature range (Fig. 3b, inset).

To corroborate this description, the experimental and theoretical TD-DFT spectra of the radical anion and the radical cation of F-spiro-NG have been obtained (Supplementary Fig. 18c). Both theoretical and experimental spectra are in very good agreement, with theoretical excitations that can be correlated with the F-spiro-NG experimental bands at 452 nm, 480 nm, 490 nm (that is, structured band as shoulders), 624 nm and 939 nm, respectively. The magnetic circular dichroism (MCD) spectra of both NGs have been recorded. In spiro-NG (Fig. 3c, bottom), the UV–visible absorption and MCD spectra contain the same number of bands (that is, with some differences in the relative intensities due to the different weights of the electric and magnetic transition dipolar moments). In the case of F-spiro-NG (Fig. 3b, top), there is a strong difference between UV–visible absorption and MCD spectra concerning the 624 nm band, which is fully absent in the MCD experiment. This result can be explained by considering that the circulation of electronic current associated with the 624-nm excitation is negligible for interfragment axial charge polarized bands, in contraposition with π–π* bands involving electron circular motion within π-conjugated frameworks of two HBC moieties.

The highest occupied molecular orbital (HOMO) and lowest unoccupied molecular orbital (LUMO) frontier molecular orbitals for spiro-NG display full wavefunction delocalization over the two HBC fragments. By contrast, the parent SOMO and SUMO orbitals in F-spiro-NG in the triplet state reveal wavefunction localization: the SOMO in the donor *t*-Bu-HBC fragment and the SUMO placed exclusively in the acceptor fluorinated HBC (Fig. 3d).

The emission spectra of these NGs in dichloromethane reveal a lower quantum yield of F-spiro-NG (2.9%) in comparison with spiro-NG (12.1%). This experimental finding can be accounted for by considering the charge-separated nature of F-spiro-NG (Supplementary Figs. 11 and 12).

The electrostatic potential map of F-spiro-NG (Fig. 3e) shows the localization of the hole (positive charge) in the centre of the donor ᵗBu-HBC moiety with a significant contribution from the spiro connecting benzenes. Meanwhile, the negative charge is mainly displaced towards the periphery or edges around the fluorine atoms in the acceptor HBC unit. This asymmetrically delocalized distribution of the hole and electron particles in the triplet state of F-spiro-NG becomes critical to maintain the charge-separated state as the most populated level, which can be connected with redox reactions where there is a blockade of the back electron transfer (that is, charge recombination) due to the segregation of the positive and negative electron densities. This fact minorizes the electronic coupling in a similar way to the back electron transfer operating in the inverted Marcus region.

Electrochemical and UV–visible–NIR spectroelectrochemical study

The voltammogram of spiro-NG presents two close oxidation processes at $E^1_{1/2\,ox} = 0.57$ V and $E^2_{1/2\,ox} = 0.78$ V (Table 1 and Fig. 4a, bottom). In the case of F-spiro-NG, the first oxidation appears at a lower potential, this is, $E^1_{1/2\,ox} = 0.42$ V, accounting for its radical-ion nature (Table 1 and Fig. 4a, top). The second oxidation wave, located at $E^2_{1/2\,ox} = 0.87$ V is explained by the lower donor character of $[F\text{-spiro-NG}]^{\bullet+}$ compared with $[spiro\text{-NG}]^{\bullet+}$, due to the pentafluorinated HBC.

On the reduction side, only one reversible process ($E^1_{1/2\,red} = -2.37$ V) is registered for spiro-NG. In the case of F-spiro-NG, three reduction processes appear: $E^1_{1/2\,red} = -0.42$ V, $E^2_{1/2\,red} = -1.53$ V and $E^3_{1/2\,red} = -2.42$ V. This justifies the ground-state radical-ion species of F-spiro-NG and its ability to undergo chemical reduction (Supplementary Fig. 29). The estimated onset potential values (Supplementary Fig. 28) allowed the calculation of the electrochemical HOMO–LUMO gap for these NGs. It is worth highlighting the narrow bandgap found in F-spiro-NG (0.63 eV) that allows, together with the bilayer structure, a thermal single electron transfer resulting in the described radical-ion pair[52].

The electrochemically formed charged species of spiro-NG (Fig. 4b) and F-spiro-NG (Fig. 4c) have been studied by UV–visible–NIR spectroelectrochemistry, performing electrolysis at constant potentials in the cathodic and anodic waves of the cyclic voltammograms. The

https://doi.org/10.1038/s41557-025-01810-2

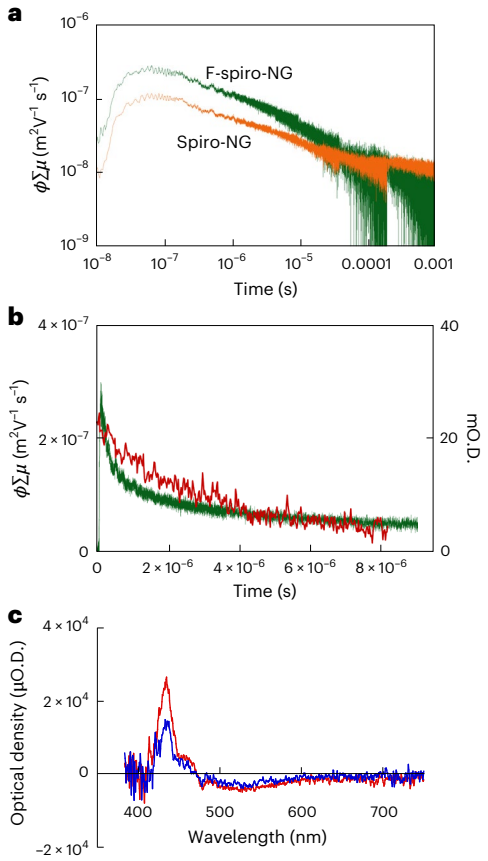

Fig. 5 | Photoconductivity. a, Global kinetic traces of differential photoconductivity recorded for spiro-NG (orange) and F-spiro-NG (green) thin solid films upon exposure to 355-nm pulses at 9×10^{14} photons cm^{-2} under ambient conditions. **b**, Kinetic traces of photoconductivity (green) and transient optical absorption at 430 nm (averaged 420–440 nm, red) recorded for an identical F-spiro-NG film upon exposure to 355 nm at 9×10^{14} and 2.1×10^{16} photons cm^{-2}, respectively. **c**, TA spectra recorded immediately (0–0.5 μs, red) and at 4 μs (4–4.5 μs, orange) after pulse exposure. mO.D., mili optical density; μO.D., micro optical density.

bands at 624 and 939 nm of the starting spectrum of F-spiro-NG (Fig. 4c, at 0 V voltage) disappear upon reduction at −0.020 V, giving rise to a spectrum with a band at 567 nm that fits well with that of the absorption spectrum of the chemically reduced species (Supplementary Fig. 29). A similar band (585 nm) is a typical signature found for photo-induced transient radical anions of perylene dimers[44]. Further oxidation of the −0.020 V species until +1 V keeps the spectrum of the starting 0 V molecule. Overoxidation at +1.5 V produces the disappearance of the above-mentioned bands. Oxidation of spiro-NG (Fig. 4b) produces the appearance of a spectrum with bands at 572, 892 and 1,123 nm unambiguously assigned to the formation of the radical cation of spiro-NG.

Electric conductive nature of spiro-NGs

Supramolecular complexes of two perylene units have demonstrated to exhibit excellent photoconductive properties[53,54]. Hence, the radical-ion character of F-spiro-NG can be favourable to produce completely dissociated free charge carriers upon external stimuli. To this end, electric conductive pathways have been examined by differential photoconductivity (direct current, d.c.) measurements with microwaves as probes for the local motion of photo-injected charge carriers (Fig. 5a)[55].

Both spiro-NG and F-spiro-NG showed evident conductivity signals with long free charge carrier lifetimes, suggesting highly conductive pathways in the solid-state aggregates. The main characteristics in these measurements are as follows: (1) the maximum conductivity was recorded at $\phi\Sigma\mu = 3 \times 10^{-7}$ m^2 V^{-1} s^{-1} in F-spiro-NG, and (2) this value in F-spiro-NG is threefold higher than the value recorded in spiro-NG. To assess the value of the mobility of photo-injected free charge carriers, transient absorption (TA) spectroscopy has been conducted for F-spiro-NG. A clear signature of radical ions was observed at 430 nm (Fig. 5c), which was in good agreement with the characteristic peaks of radical anions and cations formed by electrochemical oxidation and reduction. There were significant mismatches between the kinetic traces of d.c. and TA in the regime of 0–1 μs after excitation due to quenching of photogenerated radical anions by residual oxygen. For the long-lived species, both kinetic traces are nicely overlapped with each other at $t > 2$ μs, allowing us to estimate the mobility of the charge carriers (Fig. 5b). Given the extinction coefficient of radical cations of F-spiro-NG $\varepsilon^+ = 5.5 \times 10^4$ mol^{-1} dm^3 cm^{-1}, the value of ϕ can be calculated $\phi^+ = 5 \times 10^{-4}$, leading to an estimate of charge carrier mobility as $\Sigma\mu = 6$ cm^2 V^{-1} s^{-1} for F-spiro-NG.

Conclusions

Two molecular NGs, presenting HBCs linked through a spirobifluorene core have been prepared: (1) spiro-NG, which is decorated with ten ^{t}Bu electron-donor groups in its periphery, and (2) F-spiro-NG, which has one of the HBCs substituted with five electron-withdrawing fluorine atoms, leading to a highly polarized asymmetric system. π–π interactions within the co-facial AA-stacked HBCs, together with numerous intramolecular [C–H···π] interactions, can distort the classic orthogonal disposition of the spirobifluorene moiety to form an unexpected bilayer structure, enabling a subsequent electron-transfer event. Although photo-induced electron transfer producing transient radical-ion species has been described in multiple donor–acceptor organic systems, the persistent structure-driven electron transfer in F-spiro-NG reminds of the classical charge-transfer complexes or the modern frustrated radical pairs, made now by covalent unions. As a result, F-spiro-NG is a stable zwitterionic open-shell paramagnetic species bearing a radical cation and a radical anion. Furthermore, photoconductivity measurements show a significant increase of the charge carrier mobility in the case of F-spiro-NG ($\Sigma\mu = 6$ cm^2 V^{-1} s^{-1}) as compared with spiro-NG. The character of this unique molecule spotlights the interest in further investigating the fundamental physics behind electron donor–acceptor graphene-like systems and exploring their plausible applications in the semiconductor industry.

Online content

Any methods, additional references, Nature Portfolio reporting summaries, source data, extended data, supplementary information, acknowledgements, peer review information; details of author contributions and competing interests; and statements of data and code availability are available at https://doi.org/10.1038/s41557-025-01810-2.

References

1. Aviram, A. & Ratner, M. A. Molecular rectifiers. *Chem. Phys. Lett.* **29**, 277–283 (1974).
2. Megiatto, J. D., Guldi, D. M. & Schuster, D. I. Design, synthesis and photoinduced processes in molecular interlocked photosynthetic [60]fullerene systems. *Chem. Soc. Rev.* **49**, 8–20 (2020).
3. Wang, Z., Hu, Y., Zhang, S. & Sun, Y. Artificial photosynthesis systems for solar energy conversion and storage: platforms and their realities. *Chem. Soc. Rev.* **51**, 6704–6737 (2022).
4. Xiangjian, W., Chenxi, L., Mingtao, Z. & Yongsheng, C. Acceptor–donor–acceptor type molecules for high performance organic photovoltaics—chemistry and mechanism. *Chem. Soc. Rev.* **49**, 2828–2842 (2020).
5. Wang, J. et al. Increasing donor–acceptor spacing for reduced voltage loss in organic solar cells. *Nat. Commun.* **12**, 6679 (2021).

6. Chen, Z. et al. Evolution of the electronic structure in open-shell donor–acceptor organic semiconductors. *Nat. Commun.* **12**, 5889 (2021).
7. Li, P. et al. Exploring electronic characteristics of acceptor–donor–acceptor-type molecules by single-molecule charge transport. *Adv. Mater.* **35**, 2301876 (2023).
8. Wang, Y. et al. Designing organic mixed conductors for electrochemical transistor applications. *Nat. Rev. Mater.* **9**, 249–265 (2024).
9. Gkoupidenis, P. et al. Organic mixed conductors for bioinspired electronics. *Nat. Rev. Mater.* **9**, 134–149 (2024).
10. Ferraris, J., Cowan, D. O., Walatka, V. & Perlstein, J. H. Electron transfer in a new highly conducting donor–acceptor complex. *J. Am. Chem. Soc.* **95**, 948–949 (1973).
11. Martín, N. Tetrathiafulvalene: the advent of organic metals. *Chem. Commun.* **49**, 7025–7027 (2013).
12. Bergkamp, J. J., Decurtins, S. & Liu, S. X. Current advances in fused tetrathiafulvalene donor–acceptor systems. *Chem. Soc. Rev.* **44**, 863–874 (2015).
13. Gallego, M. et al. Complexation and electronic communication between corannulene-based buckybowls and a curved truxene–TTF donor. *Chem. Eur. J.* **23**, 3666–3673 (2017).
14. Medina Rivero, S. et al. Trapezoidal octacyanoquinoid acceptor forms solution and surface products by antiparallel shape fitting with conformational dipole momentum switch. *Angew. Chem. Int. Ed.* **60**, 17887–17892 (2021).
15. Aubry, T. J. et al. Tunable dopants with intrinsic counterion separation reveal the effects of electron affinity on dopant intercalation and free carrier production in sequentially doped conjugated polymer films. *Adv. Funct. Mater.* **30**, 2001800 (2020).
16. Kumar, S. et al. Investigation of intramolecular through-space charge-transfer states in donor–acceptor charge-transfer systems. *J. Phys. Chem. Lett.* **12**, 2820–2830 (2021).
17. Holzel, H. et al. Probing charge management across the pi-systems of nanographenes in regioisomeric electron donor–acceptor architectures. *J. Am. Chem. Soc.* **144**, 8977–8986 (2022).
18. van der Zee, L. J. C., Pahar, S., Richards, E., Melen, R. L. & Slootweg, J. C. Insights into single-electron-transfer processes in frustrated Lewis pair chemistry and related donor–acceptor systems in main group chemistry. *Chem. Rev.* **123**, 9653–9675 (2023).
19. Wang, J. et al. The Lewis acid induced formation of a stable diradical with an intramolecular ion pairing state. *J. Am. Chem. Soc.* **144**, 7978–7982 (2022).
20. Chen, X. et al. Long-lived charge-transfer state in spiro compact electron donor–acceptor dyads based on pyromellitimide-derived rhodamine: charge transfer dynamics and electron spin polarization. *Angew. Chem. Int. Ed.* **61**, e202203758 (2021).
21. Chen, X., Zhang, X., Xiao, X., Wang, Z. & Zhao, J. Recent developments on understanding charge transfer in molecular electron donor–acceptor systems. *Angew. Chem. Int. Ed.* **62**, e202216010 (2023).
22. Wang, L. & Zhu, W. Organic donor–acceptor systems for photocatalysis. *Adv. Sci.* **11**, 2307227 (2024).
23. Rickhaus, M., Mayor, M. & Juríček, M. Chirality in curved polyaromatic systems. *Chem. Soc. Rev.* **46**, 1643–1660 (2017).
24. Pun, S. H. & Miao, Q. Toward negatively curved carbons. *Acc. Chem. Res.* **51**, 1630–1642 (2018).
25. Majewski, M. A. & Stępien, M. Bowls, hoops, and saddles: synthetic approaches to curved aromatic molecules. *Angew. Chem. Int. Ed.* **58**, 86–116 (2019).
26. Reger, D. et al. A family of superhelicenes: easily tunable, chiral nanographenes by merging helicity with planar π systems. *Angew. Chem. Int. Ed.* **133**, 18221–18229 (2021).
27. Oró, A. et al. Tetrahedraphene: a C*sp*(3)-centered 3D molecular nanographene showing aggregation-induced emission. *Angew. Chem. Int. Ed.* **62**, e202312314 (2023).
28. Buendía, M., Fernández-García, J. M., Perles, J., Filippone, S. & Martín, N. Enantioselective synthesis of a two-fold inherently chiral molecular nanographene. *Nat. Synth.* **3**, 545–553 (2024).
29. Izquierdo-García, P., Fernández-García, J. M., Fernández, I., Perles, J. & Martín, N. Helically arranged chiral molecular nanographenes. *J. Am. Chem. Soc.* **143**, 11864–11870 (2021).
30. Fernández-García, J. M. et al. π-Extended corannulene-based nanographenes: selective formation of negative curvature. *J. Am. Chem. Soc.* **140**, 17188–17196 (2018).
31. Izquierdo-García, P. et al. Helical bilayer nanographenes: impact of the helicene length on the structural, electrochemical, photophysical, and chiroptical properties. *J. Am. Chem. Soc.* **145**, 11599–11610 (2023).
32. Hu, Y. et al. Spiro-fused bis-hexa-*peri*-hexabenzocoronene. *Chem. Commun.* **54**, 13575–13578 (2018).
33. Lungerich, D. et al. A strategy towards the multigram synthesis of uncommon hexaarylbenzenes. *Angew. Chem. Int. Ed.* **55**, 5602–5605 (2016).
34. Hagui, W., Doucet, H. & Soulé, J.-F. Application of palladium-catalyzed C(sp^2)–H bond arylation to the synthesis of polycyclic (hetero)aromatics. *Chem* **5**, 2006–2078 (2019).
35. Hou, I. C.-Y., Hu, Y., Narita, A. & Müllen, K. Diels–Alder polymerization: a versatile synthetic method toward functional polyphenylenes, ladder polymers and graphene nanoribbons. *Polym. J.* **50**, 3–20 (2018).
36. Kawahara, K. P., Matsuoka, W., Ito, H. & Itami, K. Synthesis of nitrogen-containing polyaromatics by aza-annulative π-extension of unfunctionalized aromatics. *Angew. Chem. Int. Ed.* **59**, 6383–6450 (2020).
37. Zhang, X., Mackinnon, M. R., Bodwell, G. J. & Ito, S. Synthesis of a π-extended azacorannulenophane enabled by strain-induced 1,3-dipolar cycloaddition. *Angew. Chem. Int. Ed.* **61**, e202116585 (2022).
38. Jin, T., Zhao, J., Asao, N. & Yamamoto, Y. Metal-catalyzed annulation reactions for π-conjugated polycycles. *Chem. Eur. J.* **20**, 3554–3576 (2014).
39. Pozo, I., Guitian, E., Pérez, D. & Peña, D. Synthesis of nanographenes, starphenes, and sterically congested polyarenes by aryne cyclotrimerization. *Acc. Chem. Res.* **52**, 2472–2481 (2019).
40. Kong, W. J., Finger, L. H., Oliveira, J. C. A. & Ackermann, L. Rhodaelectrocatalysis for annulative C–H activation: polycyclic aromatic hydrocarbons through versatile double electrocatalysis. *Angew. Chem. Int. Ed.* **131**, 6408–6412 (2019).
41. Ponugoti, N. & Parthasarathy, V. Rearrangements in Scholl reaction. *Chem. Eur. J.* **28**, e202103530 (2022).
42. King, B. T. et al. Controlling the Scholl reaction. *J. Org. Chem.* **72**, 2279–2288 (2007).
43. Izquierdo-García, P., Fernández-García, J. M., Perles, J., Fernández, I. & Martín, N. Electronic control of the Scholl reaction: selective synthesis of spiro vs helical nanographenes. *Angew. Chem. Int. Ed.* **62**, e202215655 (2023).
44. *Cambridge Structural Database* (2024).
45. Markovic, V., Villamaina, D., Barabanov, I., Daku, L. M. L. & Vauthey, E. Photoinduced symmetry-breaking charge separation: the direction of the charge transfer. *Angew. Chem. Int. Ed.* **50**, 7596–7598 (2011).
46. Vura-Weis, J., Ratner, M. A. & Wasielewski, M. R. Geometry and electronic coupling in perylenediimide stacks: mapping structure–charge transport relationships. *J. Am. Chem. Soc.* **132**, 1738–1739 (2010).

47. Kazmaier, P. M. & Hoffmann, R. A theoretical study of crystallochromy. quantum interference effects in the spectra of perylene pigments. *J. Am. Chem. Soc.* **116**, 9684–9691 (1994).
48. Manian, A. et al. Charge transfer-mediated multi-exciton mechanisms in weakly coupled perylene dimers. *Chem. Mater.* **35**, 6889–6908 (2023).
49. Sung, J. et al. Direct observation of excimer-mediated intramolecular electron transfer in a cofacially-stacked perylene bisimide pair. *J. Am. Chem. Soc.* **138**, 9029–9032 (2016).
50. Giaimo, J. M. et al. Excited singlet states of covalently bound, cofacial dimers and trimers of perylene-3,4:9,10-bis(dicarboximide)s. *J. Phys. Chem. A* **112**, 2322–2330 (2008).
51. Cook, R. E. et al. Excimer formation and symmetry-breaking charge transfer in cofacial perylene dimers. *J. Phys. Chem. A* **121**, 1607–1615 (2017).
52. Holtrop, F. et al. Photoinduced and thermal single-electron transfer to generate radicals from frustrated Lewis pairs. *Chem. Eur. J.* **26**, 9005–9011 (2020).
53. Draper, E. R. et al. Air-stable photoconductive films formed from perylene bisimide gelators. *J. Mater. Chem. C* **2**, 5570–5575 (2014).
54. Wu, N. et al. Persistent photoconductivity in perylene diimide nanofiber materials. *ACS Energy Lett.* **1**, 906–912 (2016).
55. Inoue, J. et al. Rapid evaluation of electron mobilities at semiconductor–insulator interfaces in an ambient atmosphere by a contactless microwave-based technique. *ACS Omega* **2**, 164–170 (2017).

Methods

All the information about the methodology concerning synthetic procedures, spectroscopic characterization, electrochemical measurements, DFT calculations, X-ray analysis and photoconductivity studies is reported in the Supplementary Information.

Data availability

Data that support the finding of this study can be found in the Article or its Supplementary Information. Atomic coordinates for all calculated compounds are available in Supplementary Data 1. Crystallographic data for the structures reported in this Article have been deposited at the Cambridge Crystallographic Data Centre, under deposition numbers 2338098 (spiro-NG, **4**) and 2396652 (**9**). Copies of the data can be obtained free of charge at https://www.ccdc.cam.ac.uk/structures/. Source data are provided with this paper.

Acknowledgements

N.M. and J.L.-V. thank the financial support from the Spanish MICINN (project number PID2020-114653RB-I00). N.M. and J.M.F.-G. thank the financial support by the ERC (SyG TOMATTO ERC-2020-951224). We also thank the support from the '(MAD2D-CM)-UCM' project funded by Comunidad de Madrid, by the Recovery, Transformation and Resilience Plan, and by NextGenerationEU from the European Union. D.A. acknowledges the European Union—NextGenerationEU—Maria Zambrano fellowship. J.C. acknowledges MICINN (project number PID2021-127127NB-I00) and Junta de Andalucía (project numbers PROYEXCEL-0328 and FQM-0395) for financial support. Research Central Services (SCAI) of the University of Málaga, Unidad de Espectroscopía Vibracional (C. Capel and J. L. Zafra) are also acknowledged. On the Kyoto University side, S.S. was supported by MEXT Grant-in-Aid for Scientific Research (grant numbers 20H05862, 20H05867 and 22H00314) and JST-CREST (grant number JPMJCR23O3).

Author contributions

J.L.-V., J.M.F.-G. and N.M. conceived and designed the synthesis. J.L.-V. carried out the synthetic work and performed UV–visible, emission and electrochemical experiments under the supervision of J.M.F.-G. and N.M. S.M.R. and J.C. conducted UV–visible spectroscopy, spectroelectrochemical experiments, Raman spectroscopy and MCD measurements. J.P. performed X-ray diffraction experiments. J.W. and S.W. carried out EPR measurements. S.S. conducted photoconductivity experiments. J.C. and D.A. performed theoretical calculations. J.L.-V., J.M.F.-G., S.M.R., J.C. and N.M. contributed to the interpretation of the results. All authors contributed to shaping the research, analysis and paper.

Competing interests

The authors declare no competing interests.

Additional information

Supplementary information The online version contains supplementary material available at https://doi.org/10.1038/s41557-025-01810-2.

Correspondence and requests for materials should be addressed to Juan Casado or Nazario Martín.

Peer review information *Nature Chemistry* thanks Agnieszka Nowak-Król, Alessandro Prescimone and the other, anonymous, reviewer(s) for their contribution to the peer review of this work.